Toward controlling a KUKA LBR IIWA for interactive tracking

Vinay Chawda and Günter Niemeyer

***Abstract*— In this paper we use KUKA's Fast Robot Interface (FRI) to design and implement a tracking controller on the Lightweight Robot (LBR) IIWA. We seek low latency, accurate and smooth tracking of the link positions to facilitate human interaction tasks. Focusing on a single joint and its low-level series elastic dynamics, we identify the internal torque control structure and its characteristics. Tracking controllers of varying complexity are tested in an optical motion capture system to provide an independent external reference measurement. Using full state feedback of both motor position and sensed joint torque, we achieve smooth and good tracking of the unsensed link positions.**

I. INTRODUCTION

The LBR IIWA as seen in Fig. 1 is an industrial seven degree of freedom (DOF) serial manipulator intended for human-robot collaboration. It provides internal joint torque sensing as well as suite of safety features that have allowed its certification to operate in human proximity [1], [2]. We are integrating the LBR into physical human robot interaction tasks which, at a minimum, require low latency response to a user's actions and accurate motion tracking to properly coordinate with the user.

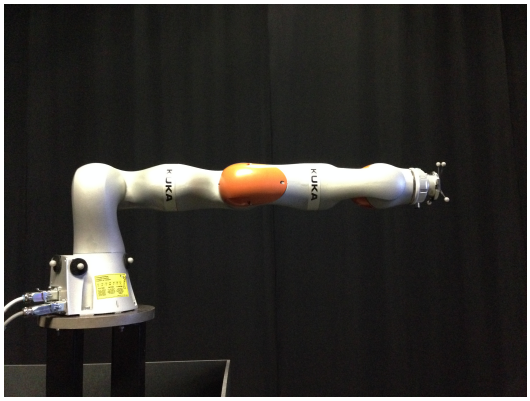

Fig. 1. KUKA LBR IIWA holding markers used for optical tracking

Unfortunately the KUKA-provided internal motion controller is designed for autonomous operations and does not facilitate real-time interaction scenarios. In Fig. 2 we see the tracking error when motion was commanded directly from the real-time optical motion capture of a user's hand movements. Errors exceeding 5cm prevented the LBR from properly aligning itself with the user.

Fortunately, KUKA provides a Fast Robot Interface (FRI) and the opportunity to implement an external controller at

Authors are with Disney Research, Glendale, CA, 91201 USA. (e-mail: vinay.chawda@disneyresearch.com, gunter.niemeyer@disneyresearch.com)

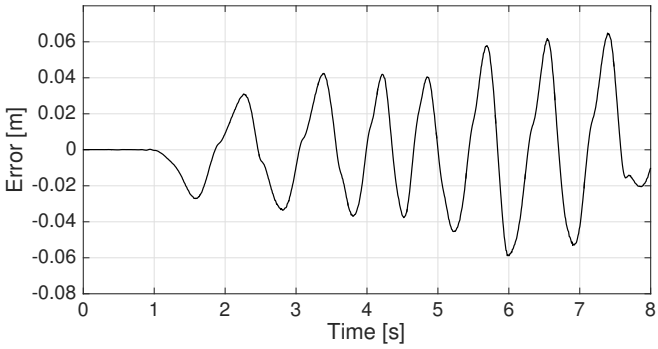

Fig. 2. Endpoint position tracking error using the LBR IIWA internal position control mode to follow a real-time motion captured hand movement.

1kHz loop rates. In this work we investigate the appropriate joint controller structure to enable real-time tracking tasks. This has to consider, in particular, the series elastic elements connecting each motor to its link and the resulting fourth order dynamics of each joint [1], [3]. Prior studies have reported the LBR IIWA's (or it's predecessor LWR 4+'s) rigid body link dynamics, under the assumption that the LBR tracks and provides link position [4], [5]. The FRI (version 1.5), however reports the motor position differing from the link position. From the base joint alone, the motor-to-link deflections can cause a 7 mm end point error. We concentrate on identifying and controlling the joint dynamics relating motor to link position, knowing that feedforward of the link inertial torques can be computed and added from existing models.

In the following, we develop the joint controller structure in the context of a single joint. We identify the system dynamics, including the transients caused by the series elasticity. We explore two-state and full-state feedback options and discuss the basic system limitations. Experiments conducted on a LBR IIWA show both good tracking as well as smooth transient response.

II. LBR IIWA OVERVIEW AND SETUP

The KUKA LBR IIWA is a serial robotic arm with seven DOF. Each joint is driven via a series elastic element connecting the motor and harmonic gear reducer to rigid links. Both motor position and joint or series elastic torques are sensed [1]. KUKA provides a Fast Robot Interface (FRI) which allows real-time control of the LBR at upto 1kHz control loop rates [6]. The FRI can be switched between position or torque control modes, accepting commands for motor position or joint torque respectively.

Under position control mode any motion commands are

passed through an internal motion interpolator before execution by an internal controller. The motion interpolator likely enforces feasible trajectories and perhaps optimizes for smoothness or similar criteria. Unfortunately, it can also introduce significant lag and nonlinearities. Fig. 3 shows the effect on a command trajectory. While it smooths the initial velocity discontinuity, it never re-converges to the intended movement. Also, the smoothing does inject an initial direction reversal. The motor position tracking itself is good, but the overall and unavoidable command-to-output lag renders this mode ill-suited for real-time tracking.

The torque control mode also passes the given torque commands through a feasibility filter. Fortunately this appears only to enforce a maximum torque slew rate. Otherwise the internal control remains quite linear and responsive, as we see in the following. We thus utilize the torque control mode to create appropriate external tracking controllers.

To evaluate our controllers and provide external reference measurements, we place the LBR inside an OptiTrack optical motion capture system. We constrain motions to the base joint so the LBR tip follows a very large arc. The motion capture resolution thus converts to an accurate measurement of the rigid body link position.

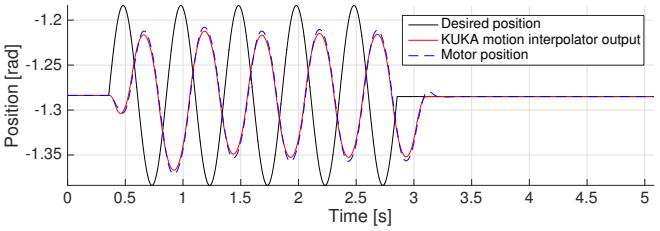

Fig. 3. Lag and filtering introduced by the LBR IIWA motion interpolator.

III. Joint Modeling

Using a lumped parameter model for a series elastic actuator ([7], [8]), the system equations for a single joint are:

$$J_m s^2 \theta_m + b_m s \theta_m = \tau_m - \tau_J \quad (1)$$

$$J_l s^2 \theta_l + b_l s \theta_l = \tau_J + \tau_{ext} \quad (2)$$

$$\tau_J = K(\theta_m - \theta_l) \quad (3)$$

where,

J_m : Motor inertia
b_m : Motor viscous friction
θ_m : Motor position
τ_m : Motor torque
τ_J : Series elastic joint torque
J_l : Link inertia
b_l : Link viscous friction
θ_l : Link position
τ_{ext} : External torque

While the linear system equations (1)-(3) describe viscous friction, we believe the actual friction to be nonlinear. The motor friction is compensated by the internal torque controller (4) and will effectively be removed from the system dynamics [9]. The link friction was identified by commanding different torques and recording steady state velocities. The nonlinear variation of torque with velocity as shown in Fig. 4 should be used in any friction feedforward. For the subsequent LTI analysis and gain tuning, however, we rely on the linear approximation.

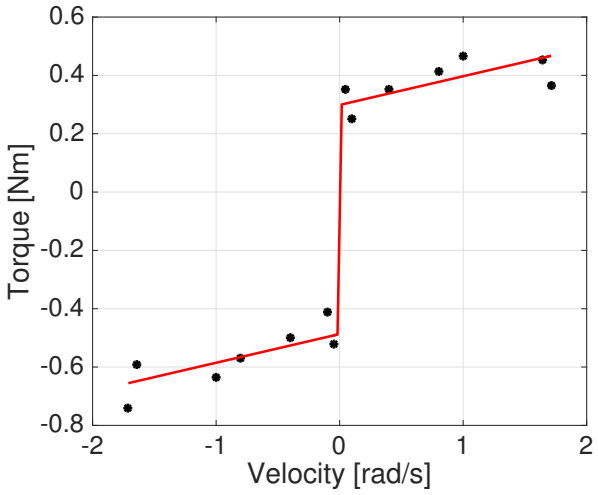

Fig. 4. Variation of measured torque with velocity shows the nonlinear friction behavior in KUKA LBR IIWA.

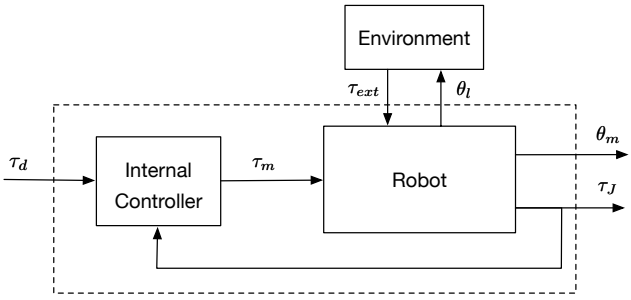

Fig. 5. Input/output signals with Fast Robot Interface for LBR IIWA

The Fast Robot Interface shown schematically in Fig. 5 outputs two sensors: motor position θ_m and joint torque τ_J. The position measurements obtained with FRI v1.5 for LBR IIWA (updated from Fast Research Interface for it's predecessor LWR 4+) are motor positions θ_m and not link positions θ_l. The OptiTrack motion capture system was used to externally measure the link position and Fig. 6 shows the differences. It can be observed that joint positions differ noticeably from the position output from the FRI. Predicting link position from (3) and both sensors, estimates more closely match the external measurements as shown in the callout.

Under torque mode, the FRI accepts torque command and internally regulates the joint torque. We approximate this controller as:

$$\tau_m = \tau_d + (K_p + K_d s)(\tau_d - \tau_J) + b_m s \theta_m \quad (4)$$

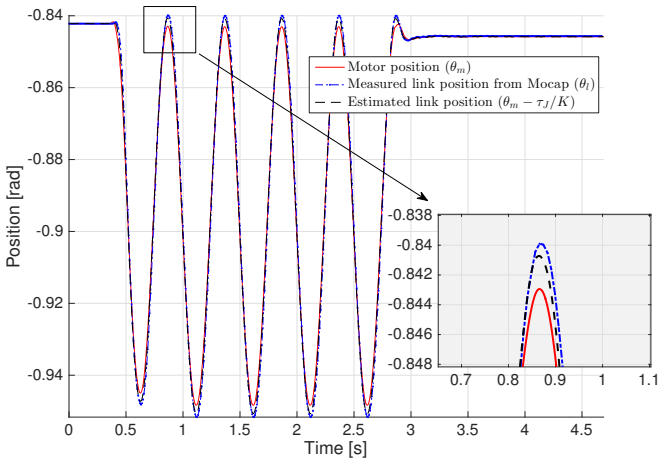

Fig. 6. Link vs. motor position

where τ_d is the commanded torque, and K_p and K_d are the proportional and derivative gains. The controller cancels the friction as best as possible, with additional unmodeled effects of internal friction and nonlinearities discussed in Section VI.

In general, we note that it is impossible to verify or identify the controller (4). Indeed substituting (4) and (3) into (1), we see

$$J_m s^2 \theta_m = (1 + K_p + K_d s)(\tau_d - K\theta_m + K\theta_l) \tag{5}$$

which we can re-write to get the internally closed loop motor dynamics

$$(J_c s^2 + b_c s + K)\theta_m = (b_c s + K)\theta_l + (b_c s + K)\frac{1}{K}\tau_d. \tag{6}$$

Here J_c and b_c are externally visible as controlled motor inertia and damping. They relate to the underlying parameters as

$$b_c = \frac{KK_d}{1+K_p} \tag{7}$$

$$J_c = \frac{J_m}{1+K_p} \tag{8}$$

The observable system is hence described by (6), (2), (3) and its parameters J_c, b_c, J_l, b_l, K are identified in the following.

IV. Parametric Identification

To identify the parameters in the system equations, we apply exponential chirps and construct experimental transfer functions from torque commands τ_d to motor position θ_m and joint torque τ_J. In particular we do this for two cases. First in free space under the assumption

$$\tau_{ext} = 0 \tag{9}$$

Second, with the flange or tip clamped. Because of compliances, this is best modelled as

$$\tau_{ext} = K_e \theta_l \tag{10}$$

where we statically measured K_e as 70000 Nm/rad. Because of the same compliances also only a portion of the inertia $J_l^* < J_l$ remains in motion, so we allow the link inertia to vary between cases.

Combining system equations (6), (2), (3) and the environment models (9) or (10), we construct the expected transfer functions in Table I. In all cases these are 4th order with a relative degree of 1, i.e. with 3 zeros. Figures 7a-7d show the experimental and parametrically fit frequency responses.

The fitted numerical values are: J_c = 1.03 kgm^2, b_c = 56.5 Nms/rad, J_l = 5.6 kgm^2, K = 18500 Nm/rad, b_l=20 Nms, J_l^*=1.4 kgm^2 and K_e = 70000 Nm/rad. Additionally, experiments were conducted with an added inertia of 3.09 kgm^2 to test the validity of identified parameters. The bode plots for the added inertia case are not presented here due to space constraints. Friction in the link is modeled as viscous friction b_l, however it is only a linear approximation as shown by the nonlinear velocity dependence of friction torque on velocity in Fig. 4.

Figures 7e and 7f show the poles and zeros for $H_{\text{free},\theta}(s)$ and $H_{\text{fixed},\theta}(s)$. Tables II and III list all the poles and zeros for free space and flange fixed cases. Beyond knowing the parametric values, several observations are of note. In the free space case we see two poles at and near the origin reflecting the center-of-mass motion. Clearly the torque mode provides no position feedback and the center of mass is free to move. The other two poles at ω_n = 146 rad/s are fast but quite underdamped. This is the controlled resonance of the series elastic and the effective motor inertia. While stable, we will see that this mode does not interact well with torque ripple during movements. Indeed the internal torque controller was likely tuned for quasi-stationary force tasks. In the zeros, we see the fast zero at ω_n = 327 rad/s introduced by the torque controller. And for $H_{\text{free},\tau}(s)$, we see two zeros masking the center of mass motion that is obviously unobservable in the torque sensor.

In the fixed case, the transfer functions, poles, and zeros are appropriately similar with the exception that the center-of-mass poles are now extremely fast, keeping the center-of-mass stationary. Indeed the high speed poles make the estimate of J_l^* rather uncertain and the bode plots really just reflect the second order dynamics of the joint torque.

V. Position Control

In this section, we develop and tune controllers of increasing complexity to reveal what elements are necessary to obtain a desirable performance. Each controller is tested on an acceleration square wave with the results collected in Fig. 8. We show the link position tracking error $\theta_{l,error} = \theta_{l,des} - \theta_l$, the motor velocity $\dot{\theta}_m$, and commanded torque τ_d. The trajectories illustrate both transients at corners and steady state tracking during motion. For reference, submitting the same desired motion to the built-in position controller results in a 0.003 rad link position tracking error.

A. PD control

We begin with the simplest Proportional-Derivative (PD) controller on motor position feedback, giving a 2-state con-

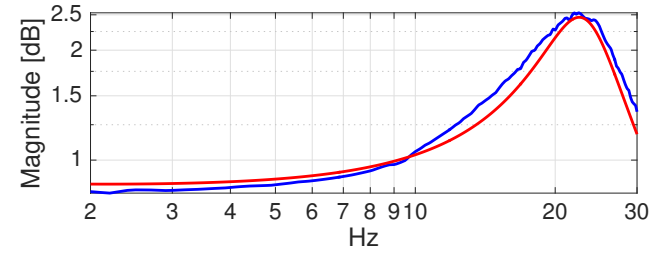

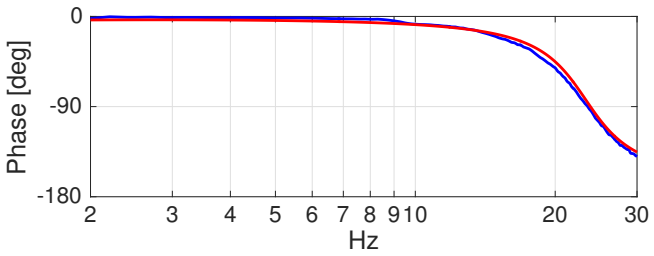

(a) $\tau_d \rightarrow \tau_J$, Free space

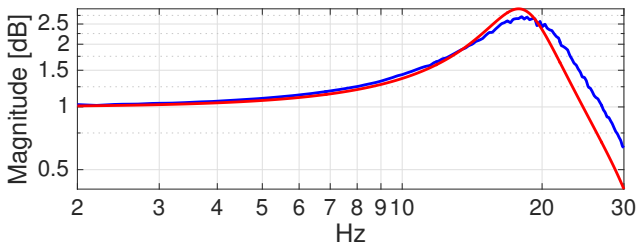

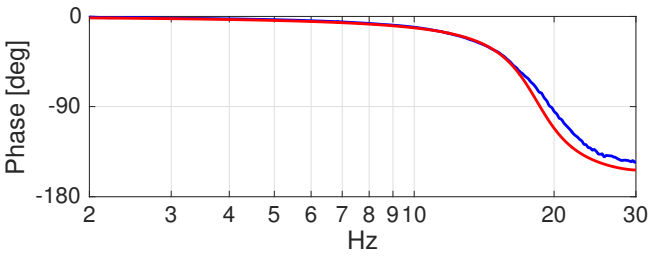

(b) $\tau_d \rightarrow \tau_J$, Flange clamped

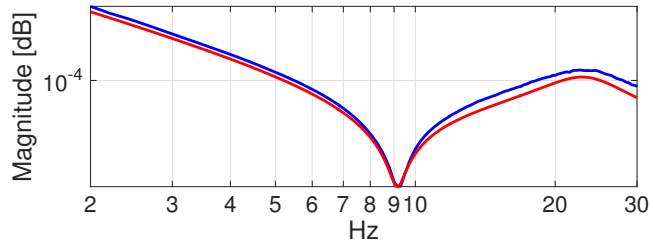

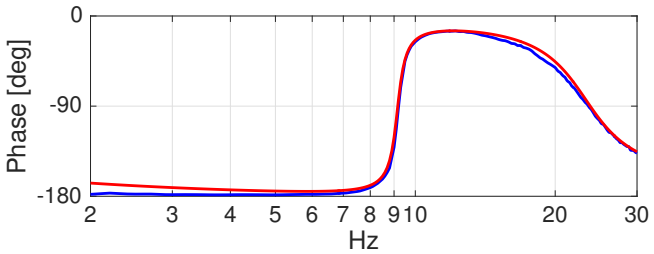

(c) $\tau_d \rightarrow \theta_m$, Free space

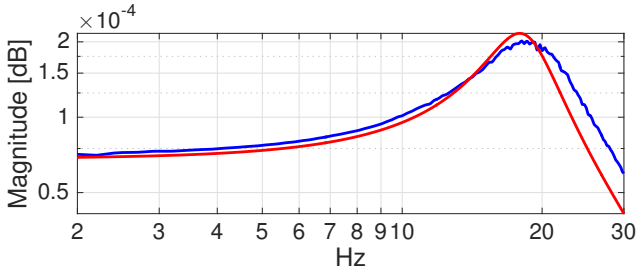

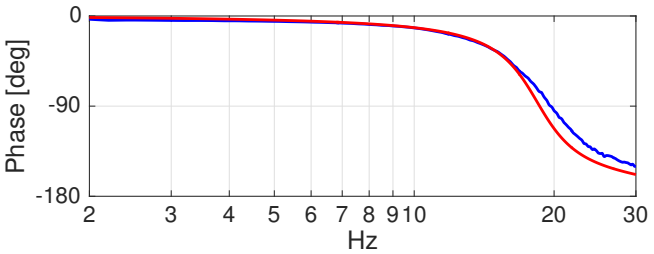

(d) $\tau_d \rightarrow \theta_m$, Flange clamped

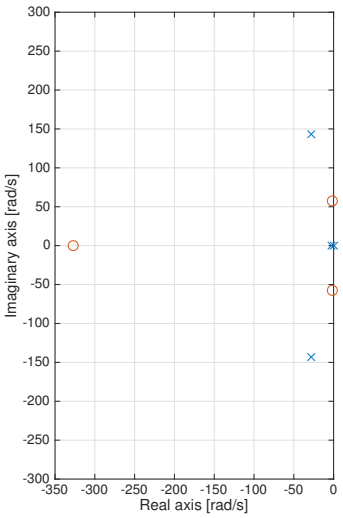

(e) Pole-zero map for $H_{\text{free},\theta}(s)$

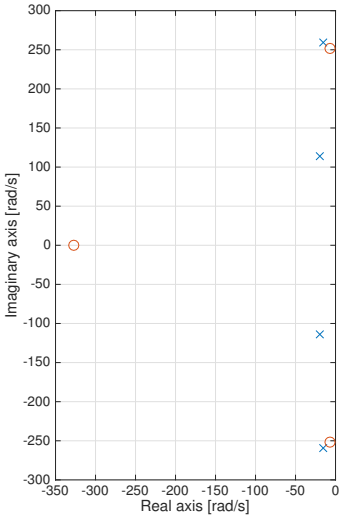

(f) Pole-zero map for $H_{\text{fixed},\theta}(s)$

Fig. 7. Frequency response and pole-zerp plots for free space motion and fixed case. The blue lines in the plots correspond to the experimental frequency responses, and the red lines correspond to the fitted transfer function response.

TABLE I

TRANSFER FUNCTIONS FOR FREE SPACE AND FLANGE FIXED CONDITIONS

$H_{\text{free},\tau}(s)$	$\frac{\tau_J(s)}{\tau_d(s)}$	$\frac{(J_l s^2+b_l s)(b_c s+K)}{J_c J_l s^4+(J_c b_l+J_l b_c)s^3+(J_c K+J_l K+b_l b_c)s^2+K b_l s}$
$H_{\text{free},\theta}(s)$	$\frac{\theta_m(s)}{\tau_d(s)}$	$\frac{(J_l s^2+b_l s+K)(b_c s+K)}{K(J_c J_l s^4+(J_c b_l+J_l b_c)s^3+(J_c K+J_l K+b_l b_c)s^2+b_l K s)}$
$H_{\text{fixed},\tau}(s)$	$\frac{\tau_J(s)}{\tau_d(s)}$	$\frac{(J_l^* s^2+b_l s+K_e)(b_c s+K)}{J_c J_l^* s^4+(J_c b_l+J_l^* b_c)s^3+(J_c K+J_l^* K+b_l b_c+J_c K_e)s^2+(K b_l+K_e b_c)s+K_e K}$
$H_{\text{fixed},\theta}(s)$	$\frac{\theta_m(s)}{\tau_d(s)}$	$\frac{(J_l^* s^2+b_l s+K_e+K)(b_c s+K)}{K(J_c J_l^* s^4+(J_c b_l+J_l^* b_c)s^3+(J_c K+J_l^* K+b_l b_c+J_c K_e)s^2+(K b_l+K_e b_c)s+K_e K)}$

TABLE II

POLE AND ZEROS OF THE IDENTIFIED TRANSFER FUNCTIONS IN FREE SPACE CONDITION.

		$\omega_n[rad/s]$	ζ
Poles:	$-27.8 \pm 143i$	146	0.19
	-3.01	3.01	
	0	0	
Zeros ($H_{\text{free},\tau}$):	-3.57	3.57	
	-327	327	
	0	0	
Zeros ($H_{\text{free},\theta}$):	$-1.79 \pm 57.4i$	57.5	0.0311
	-327	327	

TABLE III

POLE AND ZEROS OF THE IDENTIFIED TRANSFER FUNCTIONS IN FLANGE FIXED CONDITION.

		$\omega_n[rad/s]$	ζ
Poles:	$-15.4 \pm 259i$	260	0.059
	$-19.2 \pm 114i$	115	0.167
Zeros ($H_{\text{fixed},\tau}$):	$-7.14 \pm 223i$	224	0.032
	-327	327	
Zeros ($H_{\text{fixed},\theta}$):	$-7.14 \pm 251i$	251	0.028
	-327	327	

troller. We further ignore the series elasticity but add inertial feedforward

$$\tau_d = C_p(\theta_{l,des} - \theta_m) + C_d(\dot{\theta}_{l,des} - \dot{\theta}_m) + J_l \ddot{\theta}_{l,des} \quad (11)$$

The PD control gains were tuned to get the best tracking performance, and chosen as C_p=2000 Nm/rad and C_d=140 Nms/rad. Motor velocity $\dot{\theta}_m$ was computed as a filtered backward difference with a 50Hz cutoff.The closed loop poles are located at (-89.9 $\pm$ 108i, ω_n=22.3Hz, ζ=0.64), (-12.6 $\pm$ 13.3i, ω_n=2.9Hz, ζ=0.687) and (-304.7, ω_n=48.5Hz). In Fig. 8a we see reasonable tracking with some less-than-ideal oscillations in velocity and torque. In particular the 22Hz closed loop poles corresponding to the motor to series elasticity resonance are excited and resonate with the harmonic drive's torque ripple. We discuss this limitation in greater detail below, but recognize the undesirable non-smoothness.

B. PD control considering the joint stiffness

The PD control scheme (11) is modified to consider the series elasticity. The resulting augmented controller:

$$\theta_{m,des} = \theta_{l,des} - \frac{\tau_{J,des}}{K}$$
$$\tau_d = C_p(\theta_{m,des} - \theta_m) + C_d(\dot{\theta}_{m,des} - \dot{\theta}_m) + J_l \ddot{\theta}_{l,des} \quad (12)$$

where,

$$\tau_{J,des} = J_l \ddot{\theta}_{l,des} + b_l \dot{\theta}_{l,des} \quad (13)$$

again only feeds back 2 states and in fact differs only in the trajectory feedforward. Not surprisingly, Fig. 8b shows the same transients and velocity oscillations while the position tracking is $\sim$10% smaller.

C. Full state feedback control

To improve transients we next consider full state feedback (FSF)

$$\theta_{m,des} = \theta_{l,des} - \frac{\tau_{J,des}}{K}$$
$$\tau_d = C_p(\theta_{m,des} - \theta_m) + C_d(\dot{\theta}_{m,des} - \dot{\theta}_m)$$
$$+C_t(\tau_{J,des} - \tau_J) + C_u(\dot{\tau}_J) \quad (14)$$

As the interaction of the underdamped 22Hz poles with the torque ripple caused vibration issues, we deliberately bring all closed loop poles to a critically damped and slightly lower value of ω_n = (-9.5, -9.0, -7.5 and -7.0Hz). This requires the gains C_p = 2180, C_d = 157, C_t = -0.447 and C_u = 0.00023.

Fig.8c shows the resulting performance. Foremost we see a much smoother steady state in velocity and torque, where the torque ripple is no longer amplified. Of course, as the poles are slightly slower than in the PD cases, the position

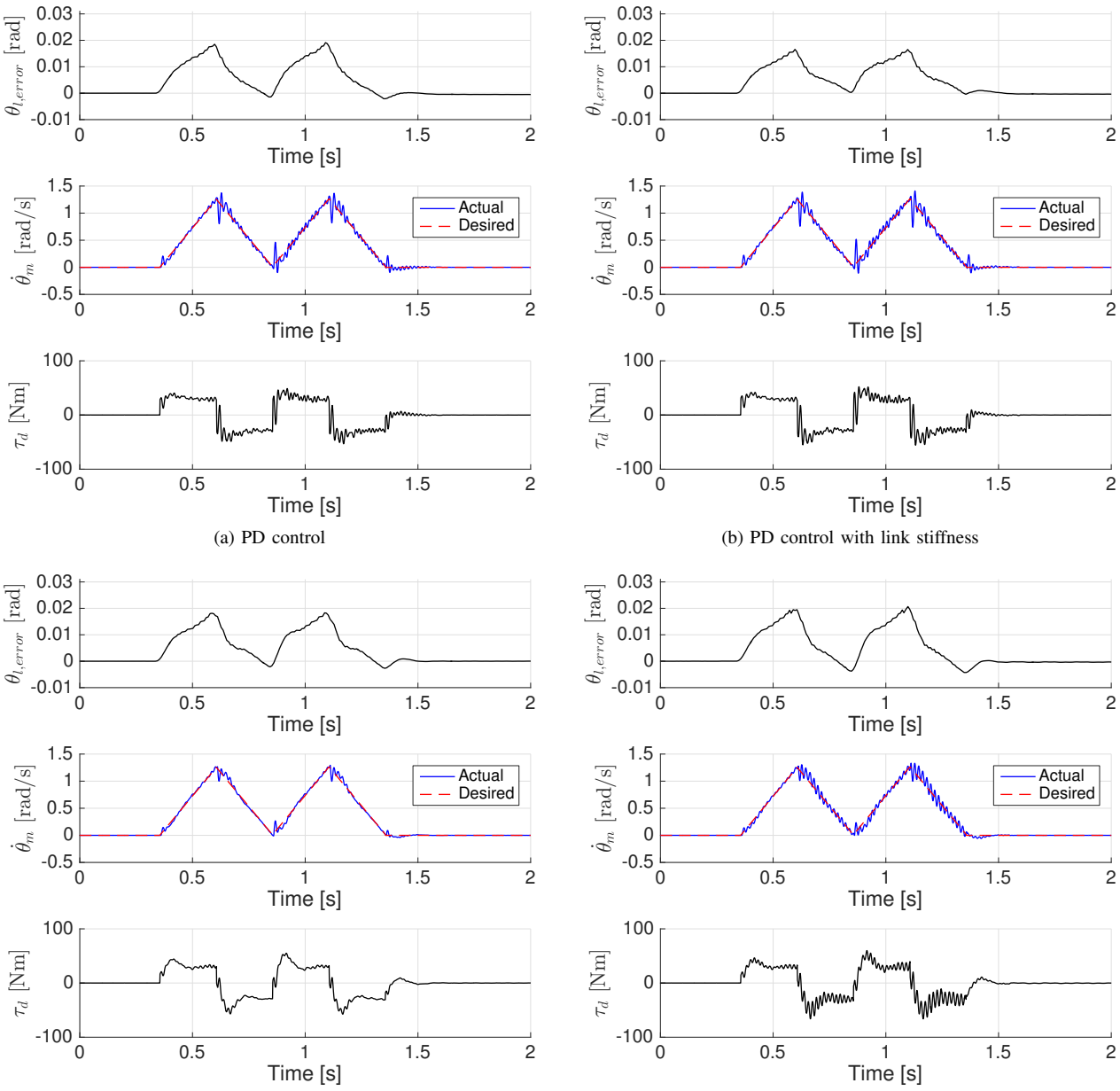

(a) PD control

(b) PD control with link stiffness

(c) FSF control

(d) Aggressive FSF control

Fig. 8. Acceleration step responses: We show the link position tracking error measured externally, the motor velocity tracking and the commanded torque in all controllers.

tracking error increases slightly. Performance approximately equals the original PD.

D. Aggressive full state feedback controller

In an effort to recapture better tracking we also try to place the closed loop poles slightly more aggressively at ω_n = (-11.5, -11.0, -7.5, -7.0 Hz). Fig.8d we see that this mostly reinstates the velocity and torque oscillations. As such we conclude that smoothness and the torque ripple dictate that the closed poles remain under 10Hz. This simultaneously bounds the tracking performance, though error levels remain $\sim$50% below the built-in position controller.

VI. Torque control limitations

We have seen that any undamped poles at frequencies above 10Hz can easily be excited by torque ripple. To confirm we take a closer look at the torque behavior. In Fig. 9 we command a slow torque ramp τ_d and observe strong oscillations or ripples in the joint torque τ_J. The ripples persist even after τ_d drops to zero and grow in magnitude upto 5 Nm before decaying to a sustained limit cycle. We also notice the change in ripple frequency which appears to increase with velocity. Plotting torque versus position shows a fixed spatial frequency, which indicates the possibility that these torque ripples are caused by the gearing in the drives.

The torque shows a second nonlinear behavior likely

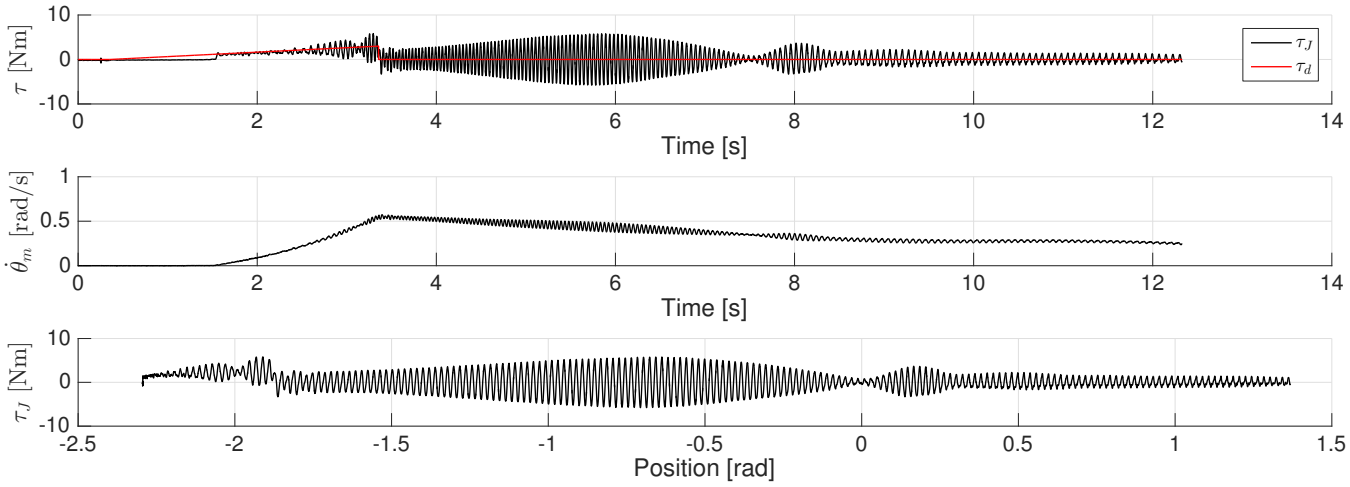

Fig. 9. Torque ripple: The torque command is slowly ramped up for 3.5s before being set to zero. Plotted against position, the torque ripple shows a fixed frequency.

associated with motor stiction or some form of deadzone or other nonlinear element in the internal friction compensation scheme. In Fig.10 we command torque ramps of varying degree (2Nm/s and 5m/s). In both cases the joint torque remains at zero until the error reaches nearly 2 Nm before vibrations and the induced dither ensue.

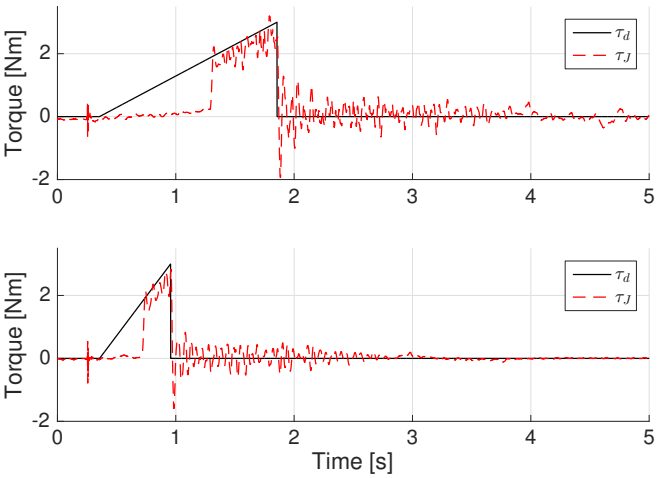

Fig. 10. Torque ramp inputs: Note the apparent stiction or deadzone that holds the sensed torque to zero.

VII. CONCLUSIONS

In this paper we examined position tracking for the KUKA LBR IIWA, especially for real-time interaction tasks. Modelling the series elasticity accounts for unreported difference between motor position and link position and improves the transient response. We find torque ripples, likely caused by the gearing, place an upper bound on the controller bandwidth and how aggressively the controller gains can be tuned while still retaining smoothness. Meanwhile motor stiction can prevent accurate control at small torque levels when stationary. Nonetheless we are able to improve the externally observed link position tracking

We believe this understanding will also help us observe and smoothly control delicate external torques during physical human-robot interactions. Ultimately we hope the improved tracking, together with contact sensing and contact regulation will make the LBR the center piece of a highly interactive and responsive system.

REFERENCES

[1] KUKA Robotics. [Online]. Available: http://www.kuka-lbr-iiwa.com

[2] S. Shepherd and A. Buchstab, "Kuka robots on-site," in *Robotic Fabrication in Architecture, Art and Design*. Springer, 2014, pp. 373–380.

[3] C. Loughlin, A. Albu-Schäffer, S. Haddadin, C. Ott, A. Stemmer, T. Wimböck, and G. Hirzinger, "The dlr lightweight robot: design and control concepts for robots in human environments," *Industrial Robot: an international journal*, vol. 34, no. 5, pp. 376–385, 2007.

[4] A. Jubien, M. Gautier, and A. Janot, "Dynamic identification of the kuka lightweight robot: Comparison between actual and confidential kuka's parameters," in *IEEE/ASME International Conference on Advanced Intelligent Mechatronics*, 2014, pp. 483–488.

[5] C. Gaz, F. Flacco, and A. De Luca, "Identifying the dynamic model used by the kuka lwr: A reverse engineering approach," in *International Conference on Robotics and Automation (ICRA)*. IEEE, 2014, pp. 1386–1392.

[6] "Kuka sunrise.connectivity fri 1.5 v3 manual," KUKA Roboter GmbH.

[7] A. Albu-Schäffer, C. Ott, and G. Hirzinger, "A unified passivity-based control framework for position, torque and impedance control of flexible joint robots," *The International Journal of Robotics Research*, vol. 26, no. 1, pp. 23–39, 2007.

[8] D. W. Robinson, J. E. Pratt, D. J. Paluska, and G. A. Pratt, "Series elastic actuator development for a biomimetic walking robot," in *IEEE/ASME International Conference on Advanced Intelligent Mechatronics*. IEEE, 1999, pp. 561–568.

[9] L. Le Tien, A. Albu-Schaffer, A. De Luca, and G. Hirzinger, "Friction observer and compensation for control of robots with joint torque measurement," in *IEEE/RSJ International Conference on Intelligent Robots and Systems*. IEEE, 2008, pp. 3789–3795.